



13th World Conference on Earthquake Engineering
Vancouver, B.C., Canada
August 1-6, 2004
Paper No. 2414

GENERATION OF NEAR-FIELD ROCK MOTIONS WITH A COMPOSITE SOURCE MODEL WITHIN THE NEW MADRID SEISMIC ZONE

**Genda CHEN¹, Mostafa EL-ENGEBAWY², Yuehua ZENG³, J. David ROGERS⁴, David
HOFFMAN⁵ and Robert B. HERRMANN⁶**

SUMMARY

In this study, the composite source model is applied to generate three-component rock motions at three bridge sites within the New Madrid Seismic Zone for various combinations of fault mechanism, moment magnitude, and distance. To take into account the uncertainties associated with the earthquake rupturing process, an equal-weight logic tree of all parameters in the composite source model is developed so that every parameter is within physical, geological, and seismological constraints. The results are validated by comparing the average of peak rock accelerations of the 100 simulations of each combination with those derived from an attenuation relation that is representative to the Central and Eastern United States. The characteristics of near-field motions are also examined.

INTRODUCTION

The New Madrid Seismic Zone (NMSZ) is the most significant regional seismic hazard in the Central and Eastern United States (CEUS). It was the location of three of the largest earthquakes (moment magnitude, M_w , of 7.5-8.0) in the United States that occurred in 1811-1812 as documented by Johnston [1] and Hough et al. [2]. Memphis and St. Louis are the metropolitan areas closest to the NMSZ where large populations, buildings, and infrastructures are exposed to significant seismic risk. The region within the

¹ Associate Professor, Department of Civil, Architectural, and Environmental Engineering, University of Missouri-Rolla, USA. Email: gchen@umr.edu

² Postdoctoral Research Associate, Department of Civil, Architectural, and Environmental Engineering, University of Missouri-Rolla, USA. Email: mostafa@umr.edu

³ Research Associate Professor, Department of Geological Sciences, University of Nevada-Reno, USA. Email: zeng@seismo.unr.edu

⁴ Associate Professor and Karl F. Hasselmann Endowed Chair in Geological Engineering, Department of Geological and Petroleum Engineering, University of Missouri-Rolla, USA. Email: rogersda@umr.edu

⁵ Geologist III, Geological Survey and Resource Assessment Division, Missouri Department of Natural Resources, Rolla, USA. Email: nrhoffd@mail.dnr.state.mo.us

⁶ Professor, Department of Earth and Atmospheric Sciences, Saint Louis University, USA. Email: rbh@eas.slu.edu

NMSZ also hosts critical infrastructures that serve local, regional, and national interests. Among those are the long-span bridge (I-155) crossing the Mississippi River at southeast of Caruthersville, Missouri, and many short-span bridges on interstate highway I-55 in southeastern Missouri. Due to lack of strong motion records in the CEUS, point-source and finite-fault models have been used to simulate the far-field motions at Memphis and St. Louis Cities induced by earthquake events in the NMSZ.

Saikai and Somerville [3] simulated the hard-rock motions at St. Louis from three large earthquakes of M_w 6.5, 7.0 and 7.5 using a finite-fault broadband time-history simulation technique. These earthquakes were considered to occur on the southwestern segment of the NMSZ. Hwang [4] used a stochastic point-source model to generate acceleration time histories at rock for a given magnitude and epicenter distance. Hwang et al. [5] propagated the simulated rock motions to the ground surface to study the seismic fragility of highway bridges in the CEUS. Toro and Silva [6] also used the stochastic point-source model to simulate ground motions for a range of site-specific soil profiles in Memphis and St. Louis. The results were utilized in constructing seismic hazard maps for the entire region including the effect of soil-column thickness, regional surficial geology, and nonlinear soil behavior. Wen and Wu [7] generated the uniform hazard rock and ground motions for Memphis, St. Louis, and Carbondale (Illinois), based on the stochastic point-source model except for M_w 8.0 where a finite-fault model was used. Suites of 10 motions were selected from a large pool of simulations such that the median of the response spectra of each suite matches that of the uniform hazard response spectrum in a least square sense at two probability levels. Atkinson and Beresnev [8] also used the finite-fault model to simulate rock and ground motions at Memphis and St. Louis from an earthquake event of M_w 7.5 that occurs on the Reelfoot fault and M_w 8.0 that occurs on the Bootheel lineament, including the linear and nonlinear amplification of representative soil profiles at each city. El-Engebawy et al. [9] simulated the rock motions at three bridge sites in the NMSZ from three large earthquakes of M_w 7.0, 7.5 and 8.0 using the finite-fault model. The sensitivity of near-field rock motions to the seismic source parameters was also investigated. Although simple, the finite-fault model can only give a single horizontal component of rock and ground motions, and thus, the near-field characteristics can not be fully captured.

Near-field motions and their associated characteristics, such as forward rupture directivity and fling step, have never been investigated within the NMSZ. The objective of this study is to generate three-component near-field rock motions in the NMSZ with the composite source model that has been validated against records from dozen earthquakes, including the 1988 Saguenay earthquake in Canada that occurred in Eastern North America's tectonic environment, earthquake faulting and geological conditions that are similar to the NMSZ. A simple logic tree is developed to take into account the uncertainties associated with the fault rupturing process and seismic wave propagation so that the synthetic rock motions generated from the composite source model are within physical, geological, and seismological constraints. The scope of the work is to generate 100 rock motions for each combination of earthquake events of M_w 6.5, 7.0 and 7.5 from two faulting mechanisms at three bridge sites. The results are validated by comparing the average of peak rock accelerations of the 100 simulations of each combination with those derived from an attenuation relation that is representative to the CEUS. The characteristics of near-field motions are also examined.

GENERATION OF NEAR-FIELD ROCK MOTIONS

Earthquake Source Parameters

Future earthquake events of M_w 6.5, 7.0 and 7.5 from rupture scenarios along the southwestern segment and the Reelfoot fault are considered as delineated in Figure 1. The southwestern segment is a vertical right-lateral strike-slip fault that is 150-200 km long as documented by Gomberg et al. [10]. Schweig and Tuttle [11] described the northwest-southeast trending Reelfoot fault as a southwest-dipping reverse fault

that is 70-80 km or even longer since its northwestern end is not well defined. For each fault and moment magnitude, the best-estimate fault dimensions and the resulting rupture area are generally determined from the empirical relations established by Wells and Coppersmith [12]. The width along the dip is constrained by Gomberg and Schweig [13] to be within the top portion (1 or 5 km) and the bottom portion (15, 20, or 33 km) of the seismogenic rupture, while the length along the strike is constrained within 20% of the plausible seismogenic length as the source parameters for large earthquakes in the NMSZ are not well understood. Other parameters such as fault coordinates, strike, etc. are taken from Dryden et al. [14]. The best-estimate parameters of each fault within the physical constraints discussed above are summarized in Table 1. Figure 1 also illustrates the location of the three bridge sites of interest along interstate highway I-55, and the estimated epicenters of the 1811-1812 New Madrid earthquakes. The closest horizontal distances from L472, A1466, and IS55 sites to the southwestern fault plane are 3.7, 10.9 and 26.5 km, respectively. The closest horizontal distances from IS55, A1466, and L472 sites to the upper edge of the Reelfoot fault are 6.3, 31.1 and 39.8 km, respectively.

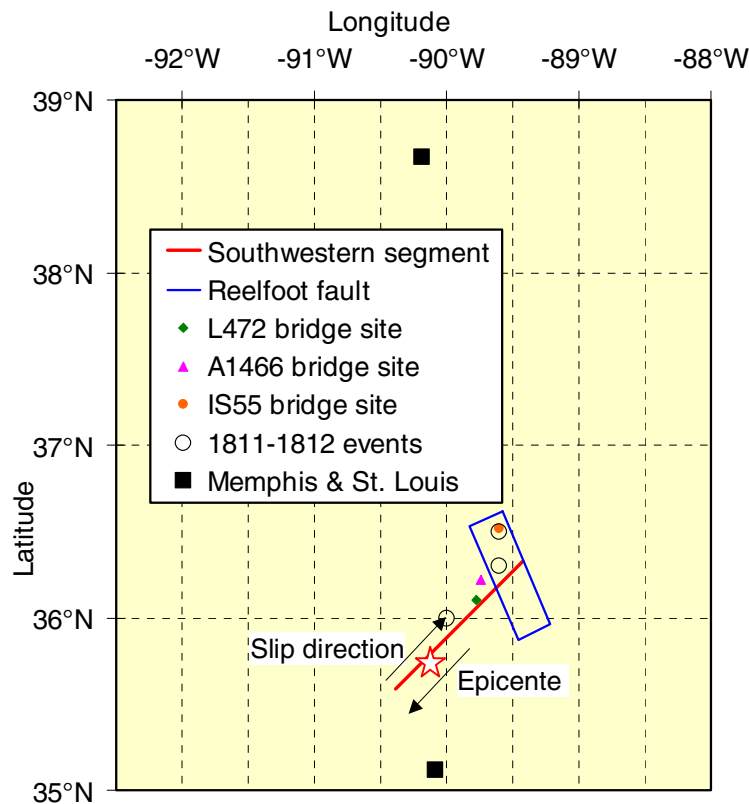


Figure 1: Overview of the study area (faults dimensions are for M_W 7.5).

Table 1: Best-estimate mechanism and dimensions of each fault.

Fault	Parameter Value
Southwestern segment (a strike-slip fault)	Strike = 226.5°, dip = 90°, rake = 180°, L = 120 km, W = 18 km for M_W 7.5, L = 56 km, W = 13.6 km for M_W 7.0, L = 27 km, W = 10 km for M_W 6.5
The Reelfoot (a reverse fault)	Strike = 156.1°, dip = 32°, rake = 90°, L = 82 km, W = 28 km for M_W 7.5, L = 44 km, W = 18 km for M_W 7.0, L = 22 km, W = 11 km for M_W 6.5
L: fault length along the strike, and W: fault width along the dip.	

The Composite Source Model

Zeng et al. [15] developed a composite source model to represent the complex fault rupturing process of an earthquake. It is assumed that the source slip function can be simulated, in a kinematic sense, by randomly distributed subevents on the fault plane, and a strong earthquake is made up of a hierarchical set of smaller earthquakes. Therefore, the source of a strong earthquake is taken as a superposition of the radiation from a significant number of circular subevents with a constant stress drop as shown in Figure 2. The subevents are allowed to overlap within the fault plane but can not extend beyond its limits. Rupture initiates at the presumed hypocenter of an earthquake event and propagates radially at a constant rupture velocity. Each subevent is triggered when the rupture front reaches the center of the subevent. The subevent then initiates the radiation of a displacement pulse according to a crack model that eventually gives the shape of Brune's pulse in the far field. The generated displacement pulse propagates through a flat multi-layered earth crust. The wave propagation process is modeled with synthetic (analytical) Green's functions in both short- and long-period ranges. Zeng [16] modified the short-period components to account for the effects of random lateral heterogeneity of the earth by adding scattered waves into the Green's functions. Because the number of subevents is substantial, the Green's functions are not computed for all of them. Rather, the fault plane is divided into a grid of approximately $4 \text{ km} \times 4 \text{ km}$ square subfaults as illustrated in Figure 2. One Green's function is determined for each subfault corresponding to the response at the site of interest due to a unit dislocation at the center of the subfault. The effect of every subevent within one subfault on the site responses is evaluated with the same Green's function with its time scale shifted by the time required for the rupture front to travel from the hypocenter to the center of the subevent and for the displacement pulse to propagate from the subevent to the site. Their effects are then added together to represent the total contribution of the subfault to the site responses.

The composite source model has been validated with records from dozen earthquakes from seven countries or regions including the United States (1979 Imperial Valley, 1989 Loma Prieta, 1992 Landers, and 1994 Northridge earthquakes), Canada (1988 Saguenay earthquake), Mexico (1985 Michoacan and Guerrero earthquakes), Japan (1995 Kobe earthquake), India (1991 Uttarkashi earthquake), Turkey (1995 Dinar and 1999 Kocaeli), and Taiwan (1999 Chi-Chi earthquake). The model can generate rock and ground motions including the synthetic prediction of the rupture directivity effect, induced from a strike-slip or reverse fault, that are in good agreement with their respective observed records as demonstrated by Zeng and Anderson [17]. Note that the Saguenay earthquake occurred in an intra-plate tectonic environment that is similar to the NMSZ, and thus it is representative to earthquakes in the NMSZ. In summary, the previous studies give one confidence that the composite source model is applicable to the NMSZ.

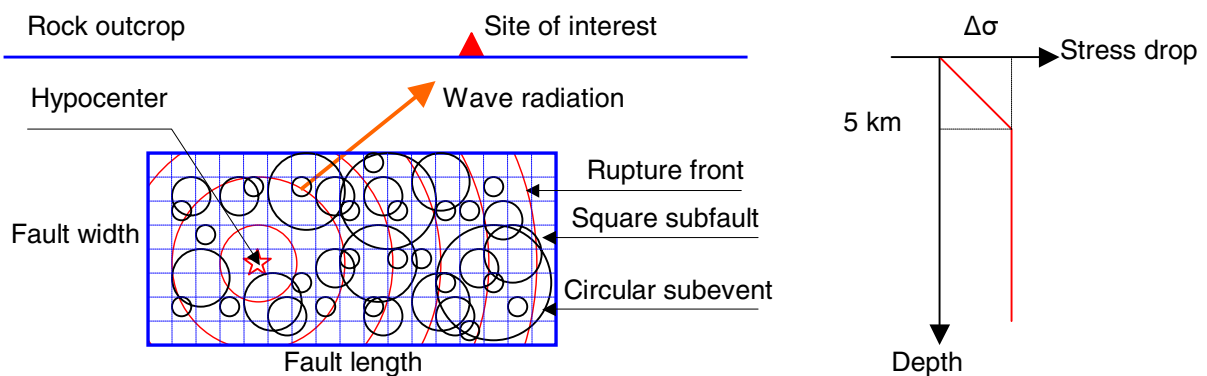
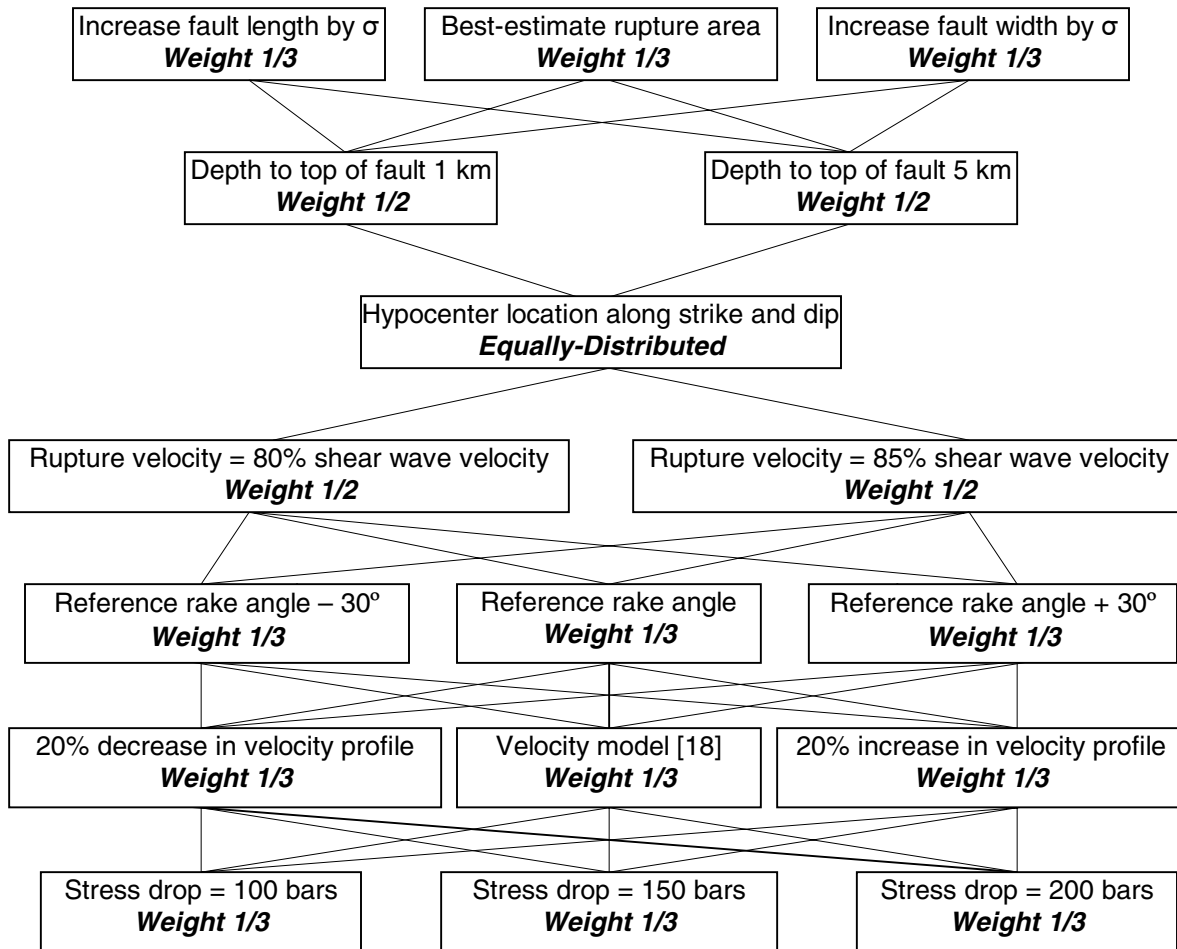


Figure 2: Idealization of the seismic source in the composite source model.

A Logic Tree of Uncertain Parameters

An emphasis is placed on the consideration of uncertainties in seismic source modeling and wave propagation. The random distributions of subevents and slip on the fault plane are considered in the composite source generation by specifying a random seed for each simulation. Additional random seeds are also introduced for each simulation to account for high-frequency wave propagation and scattering of seismic waves. For other uncertain parameters, the equal-weight logic tree shown in Figure 3 is proposed to ensure that the simulated earthquake scenarios are within physical, geological, and seismological constraints. Since numerous plausible rupture scenarios can be selected by taking one of the multiple paths from top to bottom of the logic tree and each scenario functions as a sample of a random earthquake event with variations of all key parameters in the logic tree, a probabilistic component has been introduced to the seismic source and wave propagation model.



**Figure 3: An equal-weight logic tree for characterization of uncertainties.
(Each weight means a fraction of the total number of simulations)**

In Figure 3, σ is the standard deviation of the rupture area. It is taken to be 22% of its best-estimate value for the strike-slip fault and 26% for the reverse fault as derived by Wells and Coppersmith [12]. Two alternatives for the rupture area are considered, in which one dimension is kept at its best-estimate value while the other is magnified by σ . The two branches for the depth to top of the fault are based on the top portion of the seismogenic rupture in the NMSZ given by Gomberg and Schweig [13]. The hypocenter location is equally-distributed along the strike to incorporate all rupture directivity conditions (backward and weak-to-strong forward) in the simulations. The best-estimate rupture velocity is 80% of the shear

wave velocity of the earth crust at the fault. An alternative value of 85% is also considered to account for the uncertainty in this parameter. The rake angle of the slip on the fault is 180° for a pure right-lateral strike-slip fault, and 90° for a pure reverse fault. Since a pure strike-slip or reverse faults are rare in nature, two alternatives of $\pm 30^\circ$ of the reference rake angles are considered to express their uncertainty. The reference velocity profile of the primary and secondary waves for each layer of the earth crust given by Chiu et al. [18] are also altered by $\pm 20\%$. The median stress drop in the CEUS is selected to be 150 bars as recommended by Frankel et al. [19]. A higher value of 200 bars, however, is chosen to include the possibility of occasional events with very high stress drops, for example, approximately 500 bars during the 1988 Saguenay earthquake in Canada. For M_w 7.0 (also M_w 6.5), where the rupture area is relatively small, two alternatives for its location are considered as illustrated in Figure 4. One is considered for the strong effect of forward rupture directivity at the sites of interest while the other is for the average directivity effect.

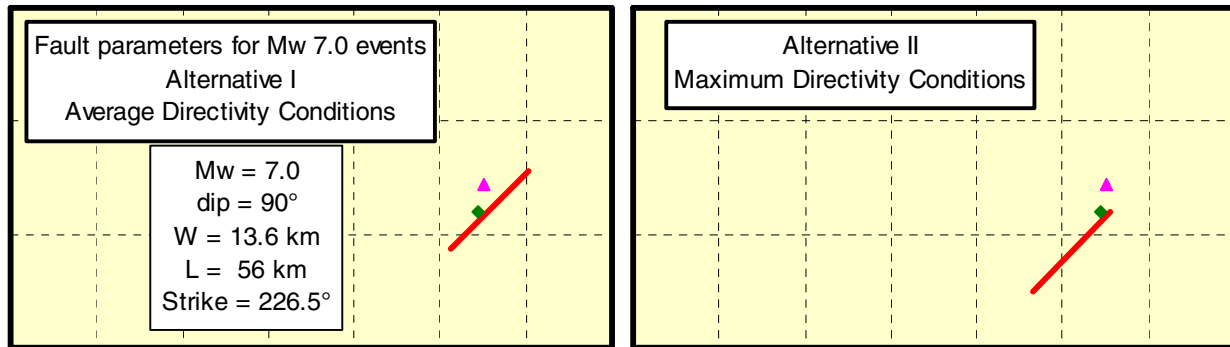


Figure 4: Two alternative locations of the southwestern segment for M_w 7.0.

SIMULATION RESULTS AND DISCUSSIONS

A total of 18 cases are considered in this study. Each is composed of one of the three bridge sites, one of the three earthquake magnitudes, and one of the two faults. For each case, 100 rupture scenarios are selected by following various paths from top to bottom of the logic tree, Figure 3, in such a way that no two identical scenarios are simulated. For each case, 100 acceleration time histories are generated and their spectral accelerations are computed for 5% damping. Further, the average response spectrum, and the ‘average plus one standard deviation’ response spectrum are also determined.

Influence of Site Location and Fault Mechanism

Four of the 18 cases are illustrated in Figures 5 and 6 for the 100 rupture scenarios of an M_w 7.0 earthquake to show the effects of fault mechanism and site location with respect to the fault. For the average response spectrum of each of the 4 cases, the spectral accelerations at critical periods as well as the peak are given in Table 2. In Table 2 and Figure 5 for rupture scenarios of the southwestern segment, the peak spectral acceleration at L472 site is 81%, 123%, and 117% higher than its corresponding values at A1466 site, for the fault-parallel (FP), fault-normal (FN), and vertical (V) components of motion, respectively. The corresponding percentages at intermediate frequencies (i.e. period 2.0sec) are reduced to -31%, 103%, and 34%, respectively. At low frequencies (i.e. period 4.0sec), the percentages are -12%, 43%, and 20%, respectively. The minus sign herein means that the fault-parallel spectral accelerations at A1466 site are larger than those at L472 site for low and intermediate frequencies; which is due to larger slip values (asperities) on the fault plane near A1466 site in most of the 100 simulations. These results indicate that the spectral accelerations in the fault-normal component of motion increase significantly for sites closer to the strike-slip fault at all frequencies, due to the forward rupture directivity effect in many of the 100 simulations.

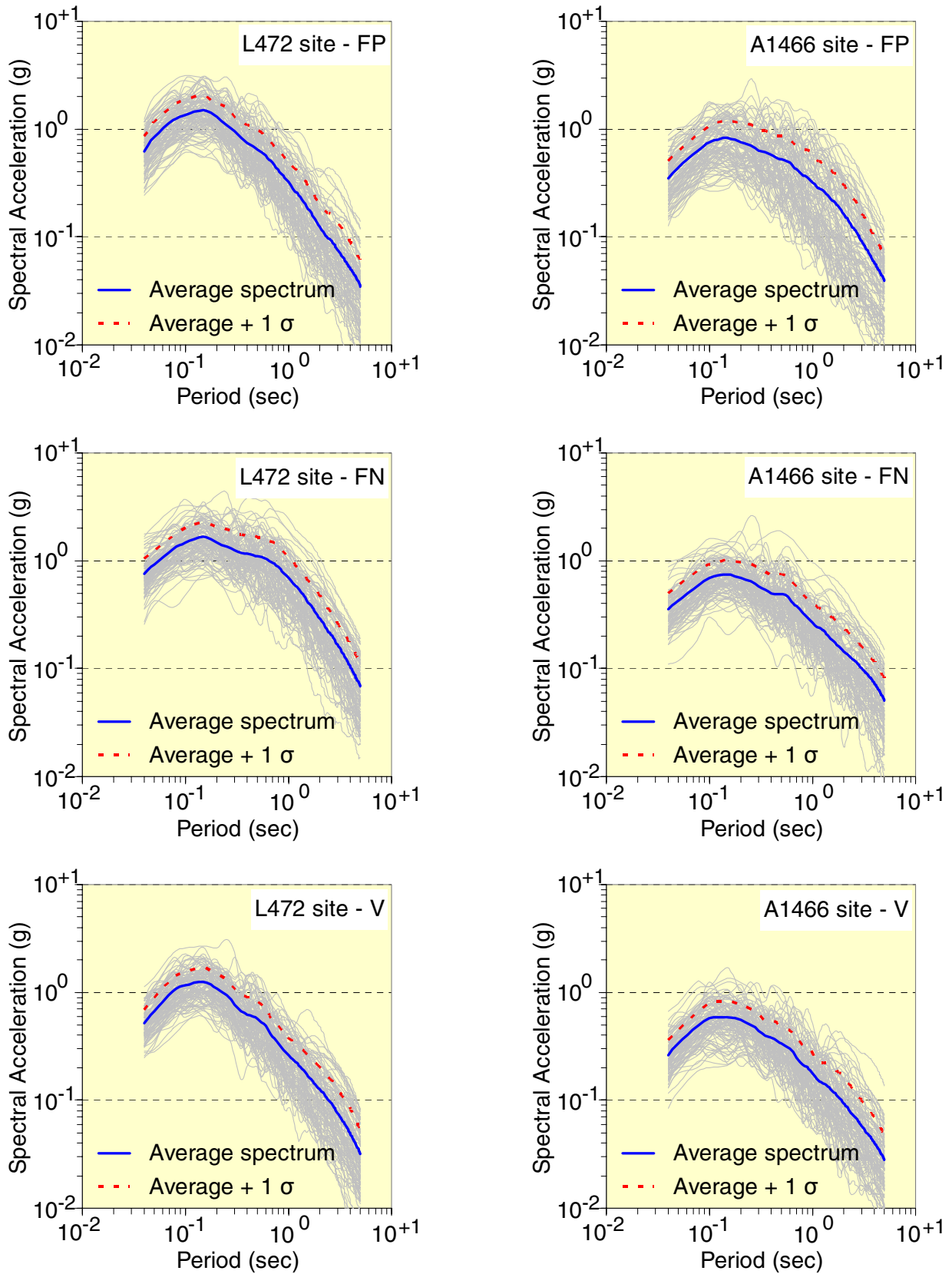


Figure 5: Results due to an M_w 7.0 event from rupture scenarios of the southwestern segment.

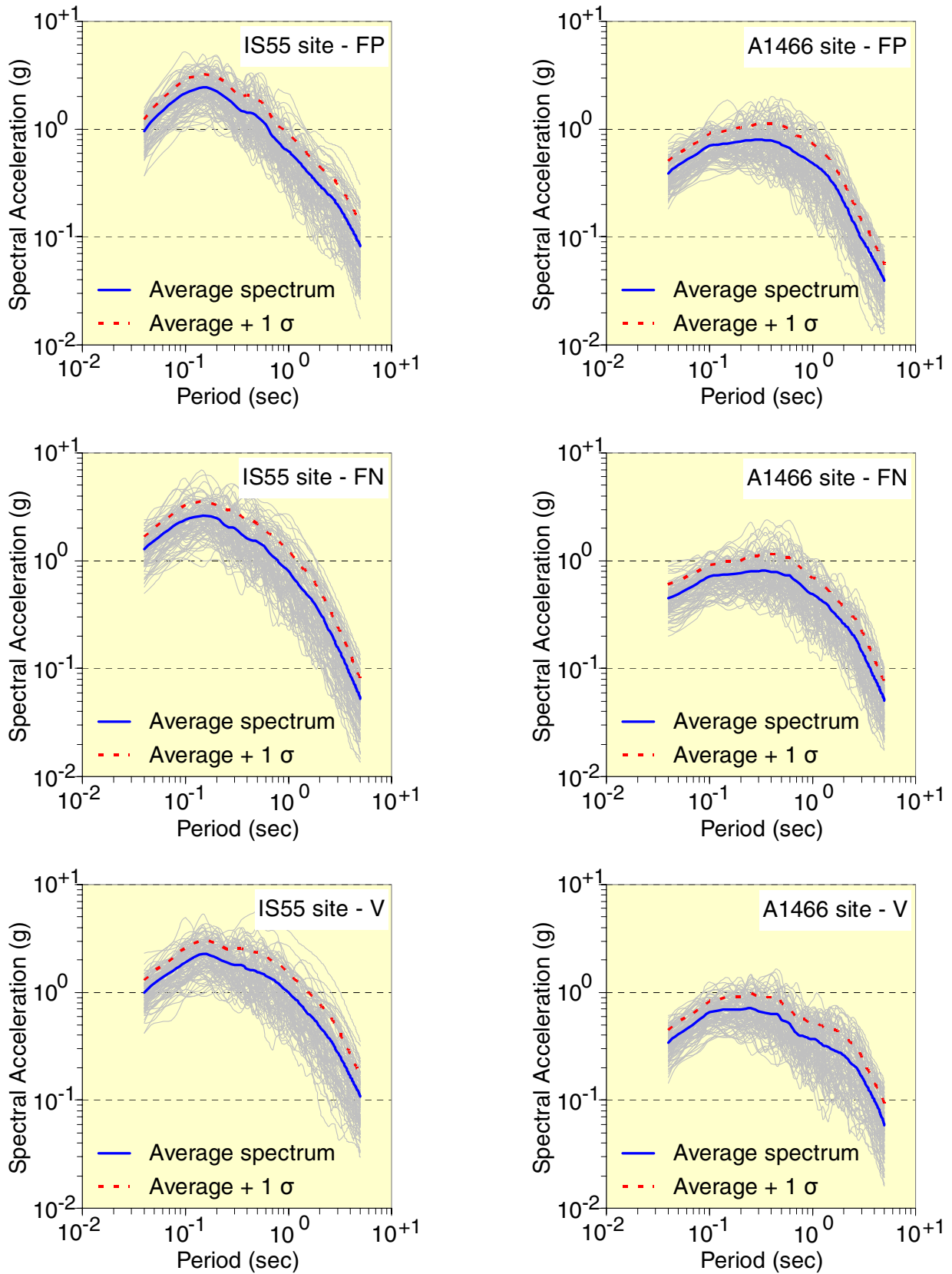


Figure 6: Results due to an M_w 7.0 event from rupture scenarios of the Reelfoot fault.

Table 2: Spectral accelerations (g) at critical periods from an M_w 7.0 earthquake.

Fault	Southwestern segment						Reelfoot fault					
Site	L472			A1466			IS55			A1466		
Motion	FP	FN	V	FP	FN	V	FP	FN	V	FP	FN	V
Peak Period	1.51 (0.15)	1.67 (0.15)	1.27 (0.15)	0.84 (0.15)	0.75 (0.15)	0.59 (0.15)	2.45 (0.15)	2.63 (0.15)	2.30 (0.15)	0.80 (0.30)	0.82 (0.35)	0.72 (0.25)
1.00	0.32	0.69	0.26	0.32	0.27	0.18	0.62	0.80	1.00	0.48	0.49	0.37
2.00	0.13	0.29	0.13	0.16	0.15	0.09	0.30	0.33	0.48	0.21	0.26	0.26
3.00	0.08	0.17	0.08	0.09	0.10	0.06	0.20	0.16	0.28	0.10	0.15	0.17
4.00	0.05	0.10	0.05	0.06	0.07	0.04	0.12	0.09	0.17	0.06	0.08	0.10

For the 100 rupture scenarios of the Reelfoot fault shown in Figure 6 and spectral acceleration values given in Table 2, the peak spectral acceleration at IS55 site is 207%, 222%, and 221% higher than its corresponding value at A1466 site, for the fault-parallel, fault-normal, and vertical components of motion, respectively. The corresponding percentages at intermediate frequencies (period 2.0sec) are reduced to 42%, 27%, and 84%, respectively. At low frequencies (period 4.0sec), the percentages are 108%, 6%, and 66%, respectively. These results indicate that the spectral accelerations increase significantly for sites located directly above the reverse fault particularly at the high-frequency component of motion (i.e. up to 0.5sec period).

The effect of fault mechanism on the average spectral accelerations is quantified by comparing the results from rupture scenarios of the southwestern segment in Figure 5 with those of the Reelfoot fault in Figure 6, in addition to the values given in Table 2. It can be observed that the average spectra of all components of motion at IS55 site from rupture scenarios of the Reelfoot fault are significantly higher than those at L472 site from the southwestern segment although their closest distances to the faults planes are quite close as given in Table 2. The peak spectral acceleration at IS55 site is 62%, 57%, and 81% higher than its corresponding value at L472 site, for the fault-parallel, fault-normal, and vertical components of motion, respectively. Further, it can also be observed that the average spectra of all components of motion at A1466 site from rupture scenarios of the Reelfoot fault are significantly higher than those from the southwestern segment although its closest distance to the Reelfoot fault is 1.77 times the corresponding distance to the southwestern segment as given in Table 2. The average spectrum of the fault-parallel component of motion is remarkably higher for period range of 0.2sec – 3.0sec with a maximum of 55% at 1.10sec, while that of the fault-normal component is significantly higher for a period range of 0.2sec – 4.0sec with a maximum of 91% at 1.40sec. The average spectrum of the vertical component is significantly higher for all periods with a maximum of 197% at 2.6sec. These results indicate the importance of considering all seismic sources in the region as their mechanisms and associated uncertainties may have a significant influence on the simulated rock motions. Finally, the vertical acceleration developed by a reverse fault mechanism is remarkably higher than that of a strike-slip fault as illustrated in Figures 5 and 6. At the peak spectral accelerations, the ratios of the vertical to the geometric mean of the two horizontal components, which is defined as the square-root of their product, are 0.80 and 0.74 at L472 and A1466 sites from rupture scenarios of the southwestern segment. The corresponding ratios are 0.91 and 0.89 at IS55 and A1466 sites from rupture of the Reelfoot fault.

Influence of Moment Magnitude

The seismic energy radiated from M_w 7.0 and 7.5 earthquakes are approximately 5.6 and 31.6 times that radiated from an M_w 6.5 earthquake. The effect of moment magnitude on the average response spectra of the fault-normal component of motion of 100 simulations is illustrated in Figure 7 for L472 and A1466 sites from rupture scenarios of the southwestern segment and in Figure 8 for IS55 and A1466 sites from rupture scenarios of the Reelfoot fault. It can be observed from Figure 7 that the spectral accelerations

increase significantly with the level of earthquake magnitude, due to the forward rupture directivity effect. The peak spectral accelerations at L472 site are 0.91g, 1.67g, and 3.73g for M_w 6.5, 7.0, and 7.5, respectively, while those at A1466 site are 0.32g, 0.75g, and 1.65g, respectively. On the other hand in Figure 8, only a slight increase is observed in the spectral accelerations at IS55 site where the peak accelerations are 2.59g, 2.63g, and 2.86g for M_w 6.5, 7.0, and 7.5, respectively. At A1466 site, however, the spectral accelerations increase significantly with the level of earthquake as the peak accelerations are 0.43g, 0.82g, and 1.74g for M_w 6.5, 7.0, and 7.5, respectively. These results are due to the location of IS55 and A1466 sites with respect to the rupture area of the Reelfoot fault as shown in Figure 1. The IS55 site is located at the northeastern corner of the fault where both fault edges are hold fixed for any level of M_w , while the two opposite edges are free to be altered to match the required rupture area corresponding to the level of M_w . As a result, the bottom edge of the Reelfoot fault approaches the A1466 site for M_w 7.5 leading to higher spectral accelerations. For IS55 site, the contribution of the subfaults close to the site has the most significant influence on the resulting time histories for all levels of M_w , while the subfaults further away from the site tend to increase the simulation durations rather than the acceleration amplitudes.

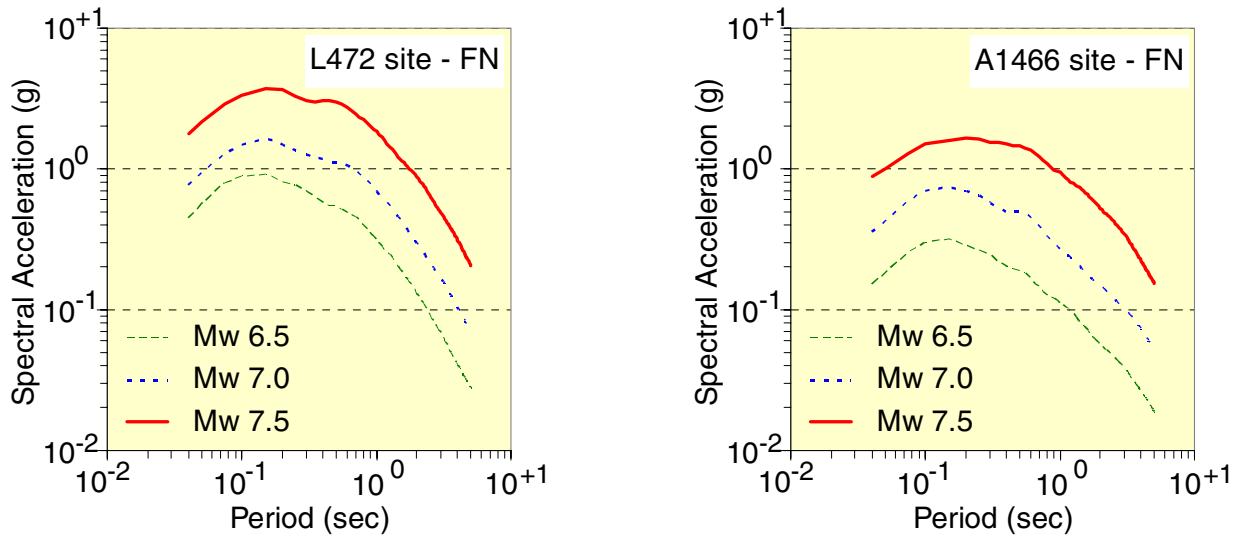


Figure 7: Influence of M_w on the average spectrum from rupture of the southwestern segment.

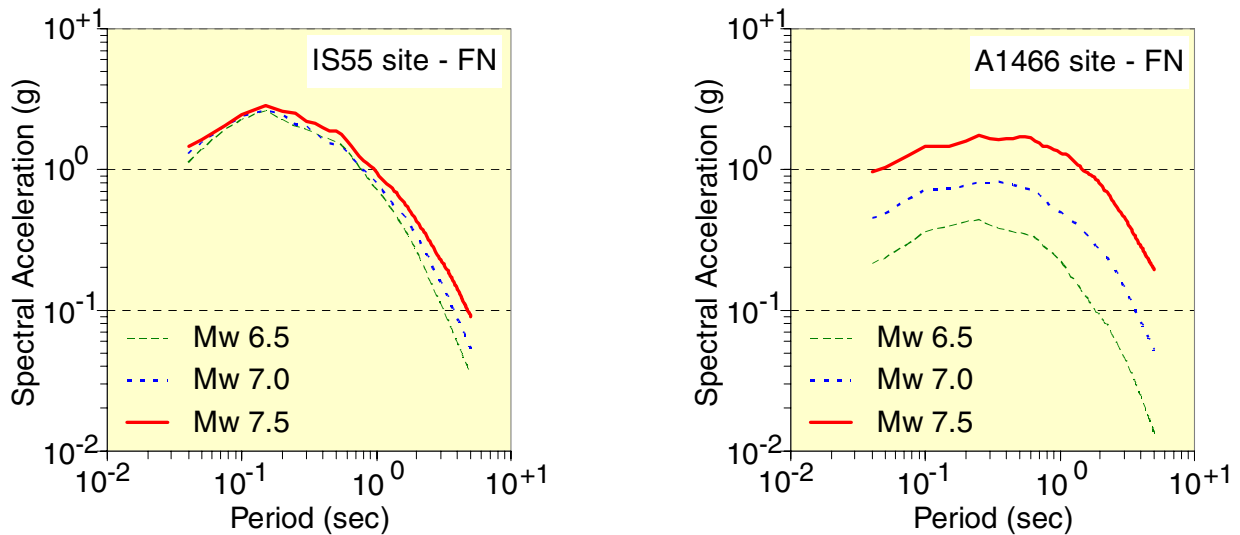


Figure 8: Influence of M_w on the average spectrum from rupture of the Reelfoot fault.

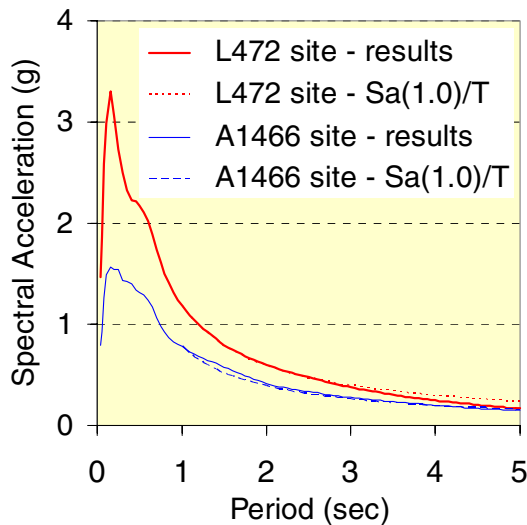
Validation of the Simulation Results

The peak rock acceleration of the geometric mean of the two horizontal components are compared in Table 3 with those computed using the attenuation relationship representative to the CEUS established by Toro et al. [20], in which the site-to-fault distance is defined as the closest horizontal distance to the vertical projection of the rupture, r_{jb} , also given in Table 3. For each case, the average of the simulated results is generally consistent with the attenuation relationship of the CEUS. For M_w 7.5, the maximum difference is 15% from rupture scenarios of the southwestern segment, and 17% from the Reelfoot fault. Further, the long period portion (beyond 1.0sec) of the average response spectra of the 100 simulations are also compared to the $S_a(1.0)/T$ decay specified in the BSSC (FEMA 302) [21] provisions, in which $S_a(1.0)$ is the spectral acceleration at 1.0sec, while T is the period. Figures 9a and 9b illustrate a comparison of the average response spectra of the simulations with the decay equation due to M_w 7.5 earthquake on the southwestern segment and the Reelfoot fault, respectively. It can be observed that the simulation results are in good agreement with the decay equation.

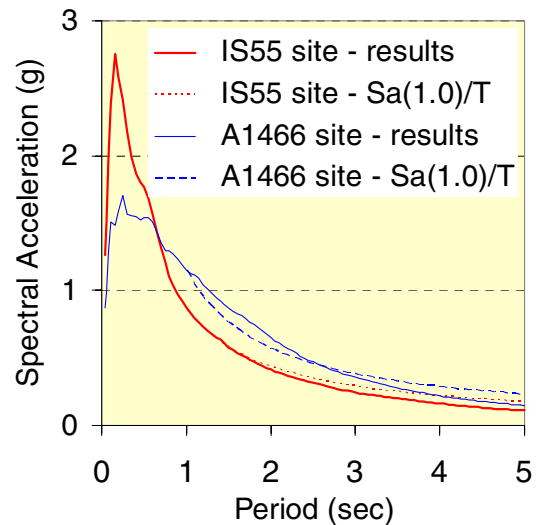
Table 3: Peak rock accelerations (g) as compared to the attenuation relation of the CEUS.

Fault	Southwestern segment				Reelfoot fault			
Site	L472		A1466		IS55		A1466	
M_w	PRA*	Toro [20]	PRA	Toro [20]	PRA	Toro [20]	PRA	Toro [20]
6.5	0.40	0.57 (3.69)**	0.16	0.36 (10.9)	1.05	0.62 (1.00)	0.20	0.19 (21.7)
7.0	0.69	0.85 (3.69)	0.36	0.54 (10.9)	1.11	0.93 (1.00)	0.42	0.39 (15.8)
7.5	1.47	1.28 (3.69)	0.79	0.80 (10.9)	1.26	1.40 (1.00)	0.88	1.03 (7.32)

* PRA: peak rock acceleration of the geometric mean of the two horizontal components.
 ** The value inside the parenthesis is distance r_{jb} .



a) Rupture of the southwestern segment



b) Rupture of the Reelfoot fault

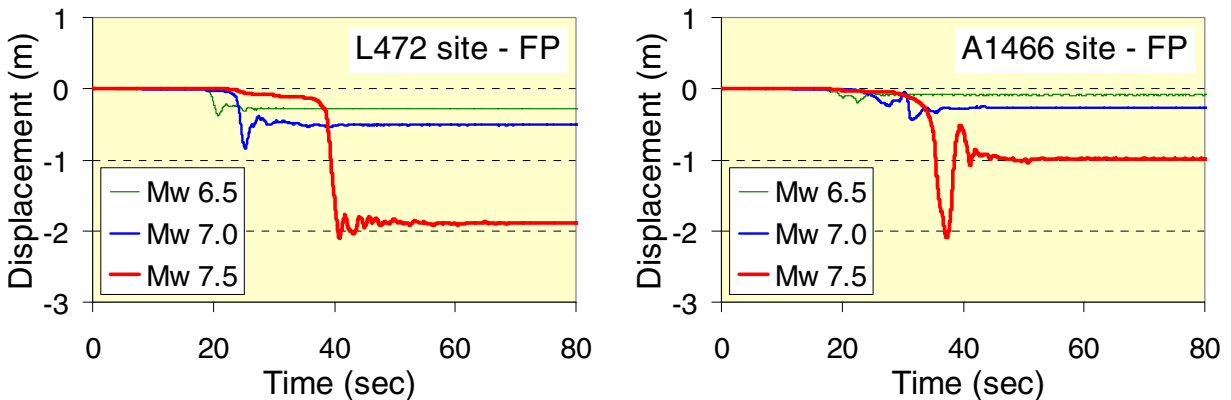
Figure 9: Comparison of the long period portion with $S_a(1.0)/T$ decay due to M_w 7.5 event.

Near-Field Characteristics of the Selected Motions

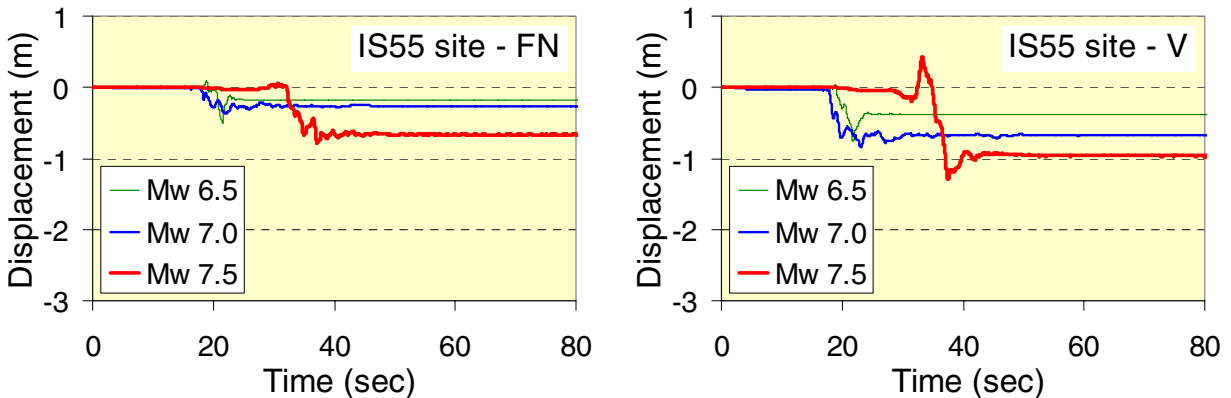
Five sets of three-component acceleration time histories are selected for each of the 18 cases such that the response spectrum of the fault-parallel, fault-normal, and vertical component of each set individually matches the average response spectrum of its corresponding 100 simulations over a period of 0.04-5.0 sec

in a least-square sense. At least one set of time histories contain distinctive velocity pulse(s) due to forward rupture directivity and one set with a large fling step. In addition, the peak rock accelerations of all selected time histories shall be within 75%-125% of the corresponding value derived from the attenuation relations established by Toro et al. [20]. The discussion on near-field effects that follows is based on the selected motions.

The influence of M_w on the permanent rock displacement (fling step on rock outcrop) is illustrated in Figure 10a for L472 and A1466 sites from rupture scenarios of the southwestern segment and in Figure 10b for IS55 site from rupture scenarios of the Reelfoot fault. For a strike-slip fault (the southwestern segment), the fling step is mainly in the direction of the slip on the fault which is in the fault-parallel component of motion. For a reverse fault (the Reelfoot), however, the slip on the fault is along the dip, and therefore, it has two components in the fault-normal and the vertical. In Figure 10a, the fling step at L472 site is 0.28m, 0.51m, and 1.89m from M_w 6.5, 7.0, and 7.5 earthquakes, respectively. The initiation time of the fling step also increase with M_w particularly for M_w 7.5. The influence of distance on the near-field characteristics is evaluated by comparing the fling step values at L472 site with the corresponding ones at A1466 site that are reduced to 0.09m, 0.26m, and 0.99m, a reduction of 32%, 51%, and 52%, respectively. In Figure 10b, the fling step at IS55 site in the fault-normal component of motion is 0.18m, 0.26m, and 0.67m, while the associated values in the vertical component is 0.39m, 0.68m, and 0.97m from M_w 6.5, 7.0, and 7.5 earthquakes, respectively. Therefore, the total fling step in the direction of the fault dip (32° from horizontal plane) is 0.36m, 0.58m, and 1.08m from M_w 6.5, 7.0, and 7.5 earthquakes, respectively.



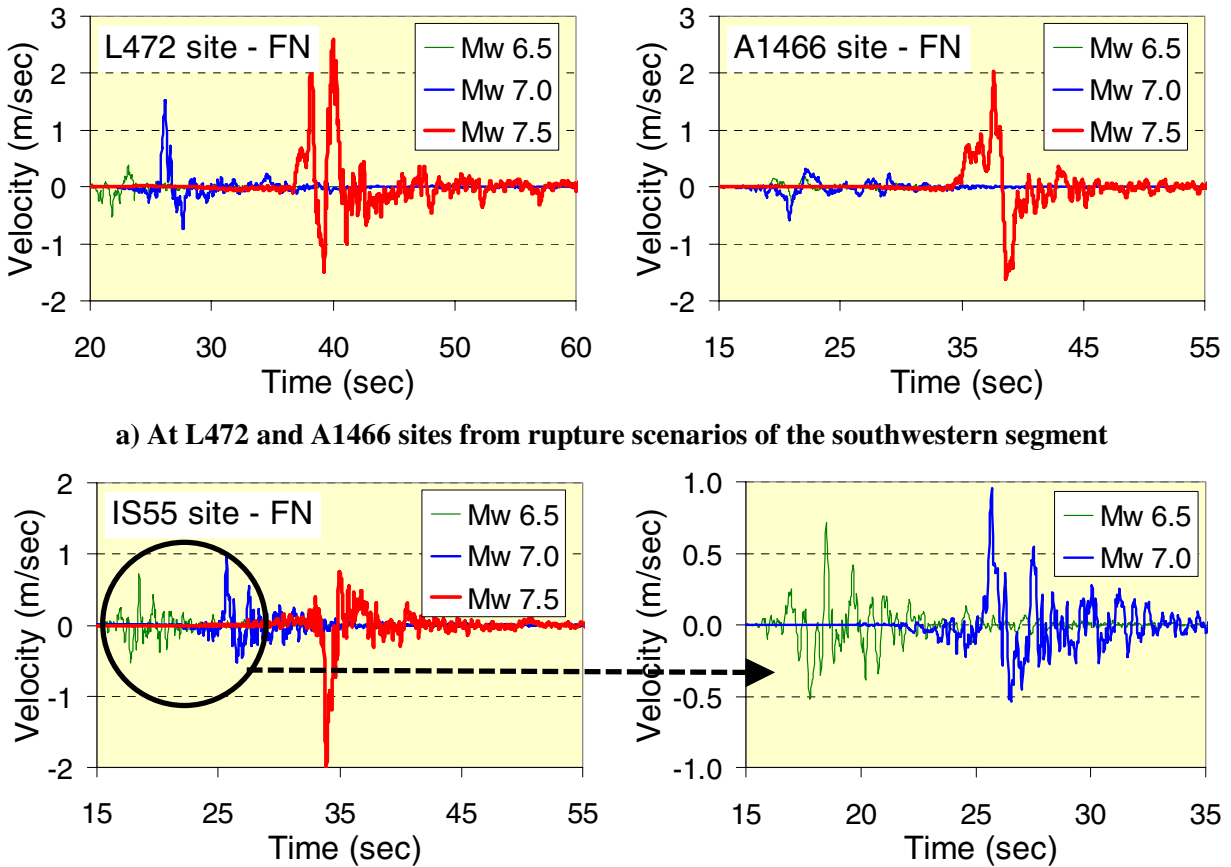
a) At L472 and A1466 sites from rupture scenarios of the southwestern segment



b) At IS55 site from rupture scenarios of the Reelfoot fault

Figure 10: Fling step for various levels of M_w .

The influence of M_w on the velocity pulse(s) is illustrated in Figure 11a for L472 and A1466 sites from rupture scenarios of the southwestern segment and in Figure 11b for IS55 site from rupture scenarios of the Reelfoot fault. In Figure 11a, the peak horizontal velocity of the fault-normal component at L472 site is 0.50m/sec, 1.48m/sec, and 2.59m/sec from M_w 6.5, 7.0, and 7.5 earthquakes, respectively. The corresponding velocities at A1466 site are reduced to 0.26m/sec, 0.60m/sec, and 2.02m/sec, a reduction of 50%, 41%, and 78%, respectively. In Figure 11b, the peak horizontal velocity of the fault-normal component at IS55 site is 0.71m/sec, 0.96m/sec, and 2.00m/sec from M_w 6.5, 7.0, and 7.5 earthquakes, respectively.



a) At L472 and A1466 sites from rupture scenarios of the southwestern segment

b) At IS55 site from rupture scenarios of the Reelfoot fault

Figure 11: Velocity pulse(s) for various levels of M_w .

CONCLUSIONS

A simple methodology has been established for the generation of three-component near-field rock motions in the NMSZ, with due considerations of the uncertainties in regional earthquake source and wave propagation characteristics. It combines the composite source model with an equal-weight logic tree that is developed to bound the uncertainties of all model parameters within physical, geological, and seismological constraints. Although the composite source model itself is deterministic, the introduction of a logic tree for various uncertainties allows one to conduct a statistical analysis of a significant number of simulations. The methodology has been used to provide rock motion time histories at three bridge sites within the NMSZ, for various combinations of moment magnitude and fault mechanism. The results have been validated against an attenuation relationship representative to the CEUS as well as the decay equation specified by FEMA 302 for the long period portion of the spectral accelerations; and found to be

in good agreement. Based on extensive simulations, the following conclusions relative to the NMSZ tectonic environment can be drawn:

1. The spectral accelerations of the three components of near-field motions increase significantly with moment magnitude and decrease with distance to the fault.
2. The fault mechanism and its associated uncertainties have a significant influence on the resulting spectral accelerations. Reverse faults (the Reelfoot) contributes more to the spectral acceleration values than the strike-slip faults (the southwestern segment), especially the vertical component of motion.
3. Near-field characteristics are more pronounced with the strike-slip fault rather than the reverse fault, due to the strong forward rupture directivity effects as a result of the site location with respect to the fault.
4. The fling step and velocity pulse(s) associated with M_w 7.5 are very large as compared to M_w 7.0 or 6.5; that would impose special demands on the seismic design of structures very close to active faults.

ACKNOWLEDGEMENTS

This study is part of a pool-funded research program on earthquake hazards mitigation for highway systems by the Federal Highway Administration, Missouri Department of Transportation, Alaska Department of Transportation, Missouri Department of Natural Resources, and the University of Missouri-Rolla under cooperative agreement DTFH61-02-X-00009. These financial supports are gratefully acknowledged.

REFERENCES

1. Johnston AC. "Seismic moment assessment of earthquakes in stable continental regions III, New Madrid 1811-1812, Charleston 1886 and Lisbon 1755." *Geophysics Journal International* 1996; 126:314–344.
2. Hough SE, Armbruster JG, Seeber L, Hough JF. "On the modified Mercalli intensities and magnitudes of 1811-1812 New Madrid earthquakes." *Journal of Geophysical Research* 2000; 105(B10):23,839–23,864.
3. Saikai CK, Somerville PG. "Simulated hard-rock motions in Saint Louis, Missouri, from large New Madrid earthquakes ($M_w = 6.5$)." *Bulletin of the Seismological Society of America* 1997; 87(1):123–139.
4. Hwang H. "Simulation of earthquake ground motion." *Proceedings of the International Conference on Monte-Carlo Simulation, Monte-Carlo, Monaco, 2001.*
5. Hwang H, Liu JB, Chiu YH. "Seismic fragility analysis of reinforced concrete bridges." *Proceedings of the 8th International Conference on Structural Safety and Reliability, Newport Beach, California, 2001.*
6. Toro GR, Silva WJ. "Scenario earthquakes for Saint Louis, MO, and Memphis, TN, and seismic hazard maps for the Central United States Region including the effect of site conditions." Report prepared for USGS by Risk Engineering Inc.; 2001.
7. Wen YK, Wu CL. "Uniform hazard ground motions for Mid-America cities." *Earthquake Spectra* 2001; 17(2):359–384.
8. Atkinson GM, Beresnev IA. "Ground motions at Memphis and St. Louis from M 7.5–8.0 earthquakes in the New Madrid Seismic Zone." *Bulletin of the Seismological Society of America* 2002; 92(3):1015–1024.
9. El-Engebawy M, Chen G, Rogers JD, Hoffman D, Herrmann RB. "Finite fault modeling of near-field rock motions in the New Madrid Seismic Zone." Provisionally accepted for publication in the *Journal of Earthquake Engineering.*
10. Gomberg JS, Atkinson GM, Bakun WH, Bodin PA, Boore DM, Cramer CH, Frankel AD, Gasperini P, Hanks TC, Herrmann RB, Hough SE, Johnston AC, Kenner SJ, Langston CA, Linker M, Mayne

- PW, Petersen MD, Powell CA, Prescott WH, Schweig ES, Segall P, Stein SA, Stuart WD, Tuttle MP, VanArsdale RB. "Reassessing the New Madrid Seismic Zone." *EOS* 2000; 81(35):397,402–403.
11. Schweig ES, Tuttle MP. "New Madrid Source Characterization." USGS Workshop 2000; Center for Earthquake Research and Information (CERI), University of Memphis, Memphis, Tennessee, 20–21 January. (www.ceri.memphis.edu/usgs/hazmap/meetings/min1_20_00.shtml)
 12. Wells DL, Coppersmith KJ. "New empirical relationships among magnitude, rupture length, rupture width, rupture area, and surface displacement." *Bulletin of the Seismological Society of America* 1994; 84(4):974–1002.
 13. Gomberg JS, Schweig ES. "A 'Strawman' logic tree for the New Madrid Seismic Zone." Memphis / Shelby Hazard Mapping Project, Center for Earthquake Research and Information (CERI), University of Memphis. (www.ceri.memphis.edu/usgs/hazmap/hazmap.shtml)
 14. Dryden M, Ellis MA, VanArsdale RB. "A model for the long-term deformation of the New Madrid Seismic Zone and surrounding region." Mid-America Earthquake Center 2001; Project SG-6 of the Regional Damage Synthesis Program – Characterization of Seismic Sources in and around the New Madrid Seismic Zone. (mae.ce.uiuc.edu/Education/Student/Graduate/SCOJ/V2N2/MDryden.pdf)
 15. Zeng Y, Anderson JN, Yu G. "A composite source model for computing realistic synthetic strong ground motions." *Geophysical Research Letters* 1994; 21(8):725-728.
 16. Zeng Y. "A realistic synthetic Green's function calculation using a combined deterministic and stochastic modeling approach." *EOS, Transactions of AGU* 1995; 76(F357).
 17. Zeng Y, Anderson JG. "Evaluation of numerical procedures for simulating near-field long-period ground motions using Zeng method." PEER Utilities Program; Report No. 2000/01.
 18. Chiu JM, Johnston AC, Yang YT. "Imaging the active faults of the central New Madrid Seismic Zone using PANDA array data." *Seismological Research Letters* 1992; 63:375–393.
 19. Frankel A, Mueller C, Barnhard T, Perkins D, Leyendecker E, Dickman N, Hanson S, Hopper M. "National Seismic-Hazard Maps: Documentation." U.S. Geological Survey: Open-file Report 96-532, June 1996; 1–110.
 20. Toro GR, Abrahamson NA, Schneider JF. "Model of strong ground motions from earthquakes in the central and eastern North America: best estimates and uncertainties." *Seismological Research Letters* 1997; 68(1):41–57.
 21. Building Seismic Safety Council. "NEHRP recommended provisions for seismic regulations for new buildings and other structures, part I: provisions (FEMA 302)." BSSC, 1997.